Nanoscale Advances

ROYAL SOCIETY OF CHEMISTRY

PAPER

View Article Online
View Journal | View Issue

Cite this: *Nanoscale Adv.*, 2020, **2**, 3209

Synergetic effects of thymoquinone-loaded porous PVPylated Fe_3O_4 nanostructures for efficient pH-dependent drug release and anticancer potential against triple-negative cancer cells†

Selvaraj Rajesh Kumar,[a] Ramar Thangam,[b] Raju Vivek,[c] Sivasubramanian Srinivasan[b] and Nagamony Ponpandian *[a]

Porous iron oxide nanostructures have attracted increasing attention due to their potential biomedical applications as nanocarriers for cancer and many other therapies as well as minimal toxicity. Herbal anti-cancer agent thymoquinone loaded on Fe_3O_4 nanoparticles is envisaged to offer solution towards cancer treatment. The purpose of the present study was to investigate the efficacy of thymoquinone-loaded PVPylated Fe_3O_4 magnetic nanoparticles (TQ-PVP-Fe_3O_4 NPs) against triple-negative breast cancer (TNBC) cells. The porous PVPylated Fe_3O_4 NPs were prepared by a simple solvothermal process, whereas the thymoquinone drug was loaded *via* the nanoprecipitation method. Fourier transform infrared (FTIR) spectroscopic analysis confirmed the molecular drug loading, and surface morphological observation further confirmed this. The quantity of thymoquinone adsorbed onto the porous PVPylated Fe_3O_4 NPs was studied by thermogravimetric analysis (TGA). The positive surface charge of TQ-PVP-Fe_3O_4 NPs facilitates the interaction of the NPs with cancer (MDA-MB-231) cells to enhance the biological functions. In addition, the anticancer potential of NPs involving cytotoxicity, apoptosis induction, reactive oxygen species (ROS) generation, and changes in the mitochondrial membrane potential ($\Delta\Psi_m$) of TNBC cells was evaluated. TQ-PVP-Fe_3O_4 NP-treated cells effectively increased the ROS levels leading to cellular apoptosis. The study shows that the synthesized TQ-PVP-Fe_3O_4 NPs display pH-dependent drug release in the cellular environment to induce apoptosis-related cell death in TNBC cells. Hence, the prepared TQ-PVP-Fe_3O_4 NPs may be a suitable drug formulation for anticancer therapy.

Received 28th March 2020
Accepted 3rd June 2020

DOI: 10.1039/d0na00242a

rsc.li/nanoscale-advances

1. Introduction

Cancer is one of the most prominent diseases caused by abnormal growth of cells and still the major public health problem with growing incidences and mortality rate. The available chemotherapeutic drugs are widely used to treat only the final stage, and in addition, they induce numerous side effects.[1,2] Therefore, there is a critical need for the development of an innovative new drug delivery system with desirable biocompatibility to treat cancer with no or minimal adverse effects.[3] Loading of therapeutic agents on nanoparticles (NPs) *via* appropriate surfactants or linkers might be a possible solution to effectively enhance the drug delivery to the specific site.[4] Herein, magnetic Fe_3O_4 NPs with superparamagnetic properties possess numerous benefits due to their biocompatibility and less toxicity. Furthermore, these magnetic NPs have preferable features such as water solubility, colloidal stability, high yields, cost effectiveness and eco-friendliness.[5] Moreover, they have the ability to transport and deliver the payloads in the desired sites using surface-exposed magnetic field and diminish the toxicity towards healthy tissue per cells.[6] Similarly, the monodisperse Fe_3O_4 NPs have an affinity to accumulate specifically in cancer tissues per cells.

During preparation, pure Fe_3O_4 NPs aggregate due to the strong magnetic interaction between the particles. Besides, the lack of functional groups on their surface limits their biological applications.[7] Hence, the magnetic NPs require possible surface modifications to become targeted drug delivery systems.[8,9] Biocompatible polymers such as polyvinylpyrrolidone (PVP), dextran, polyethylene glycol (PEG), and chitosan can be used to surface functionalize the magnetic particles, which can serve as drug carriers capable of releasing the loaded drugs or molecules

[a]*Department of Nanoscience and Technology, Bharathiar University, Coimbatore 641046, India. E-mail: ponpandian@buc.edu.in; Fax: +91-422-2422-397; Tel: +91-422-2428-421*

[b]*Department of Virology, King Institute of Preventive Medicine & Research, Chennai 600032, India*

[c]*Department of Zoology, Bharathiar University, Coimbatore 641046, India*

† Electronic supplementary information (ESI) available. See DOI: 10.1039/d0na00242a

to the specific site.[10,11] Among those, PVP is a widely used polymer due to its effective usage towards clinical applications especially for pH-dependent drug release and is considered as a more favorable biocompatible polymer for loading novel drugs.[12] Thereby, in the present study, we preferred to use this polymer for the surface encapsulation of Fe_3O_4 nanoparticles for carrying anticancer drugs.

Thymoquinone (2-isopropyl-5-methylbenzo-1,4-quinone) is a naturally occurring active herbal molecule and a constituent of volatile oil derived from the *Nigella sativa* seeds, which is used for treating many diseases.[13,14] It also possesses other beneficial activities such as antibacterial, anti-inflammatory, antidiabetic, antioxidant, analgesic, anti-ulcerogenic, anti-carcinogenic, anti-arthritic, anti-neoplastic, anti-mutagenic and antitumor functions *via* different mechanisms.[15–17] Moreover, it enhances the activities of superoxide dismutase (SOD), catalase, glutathione, glutathione transferase and quinone reductase due to their antioxidant properties.[18,19] Besides, the antitumor effects of thymoquinone on blood, lungs, breast, pancreas, colon, prostate, bone, brain, skin, ovaries, head and neck, liver, cervix and liver are reported in the literature.[17,20] In addition, thymoquinone shows manifold functions; moreover, the mechanism depends on cellular microenvironments. It has several functional activities against cancer cells including cell cycle arrest, DNA damage, ROS generation, preventing NFκB activation and induced cellular apoptosis.[14,21] In addition, in breast cancer cells it increases the cell cycle arrest due to their direct interaction with phases of G0/G1 and G2/M and induces apoptosis *via* the activation of the caspase pathway.[22] Further, it is employed in *in vivo* animal models for the treatment of acute respiratory distress syndrome and also considered to be a potential therapeutic agent for inhibiting tumor angiogenesis and tumor growth.[23,24] Thymoquinone also induces erythrocyte oxidative stress and haematological alterations during colon cancer promotion.[24,25] The active effects of thymoquinone on the improvement of targeting cell signaling and survival pathways to resist the cancer cell growth as well as to show better bioactivities were confirmed.

However, the thymoquinone drug has limitations such as poor performance with regard to aqueous solubility, biocompatibility and cell or tissue targeted activity, which hamper its therapeutic use. Therefore, the present study focuses on the development of surface-modified porous magnetic nanoparticles carrying thymoquinone for effective anticancer applications overcoming the above limitations.

In this study, the porous PVPylated Fe_3O_4 magnetic nanoparticles were prepared by a solvothermal process and the herbal-based thymoquinone drug was loaded *via* the nanoprecipitation method. This porous magnetic nanocarrier possibly improves the drug loading and releases the drug under acidic conditions prevailing in the tumor cellular environment. The physico-chemical, surface and morphological properties of the formulated pure Fe_3O_4 NPs and TQ-PVP-Fe_3O_4 NPs were discussed. Furthermore, the anticancer-associated cellular functions of these TQ-PVP-Fe_3O_4 NPs were studied in MDA-MB-231 (Scheme 1). The obtained results clearly indicated the ability of the prepared TQ-PVP-Fe_3O_4 NPs to display effective nanodrug delivery functions in cultured MDA-MB-231 cells and significantly improve the anticancer efficacy by inducing apoptosis-related factors. Hence, we envision that the features of TQ-PVP-Fe_3O_4 NPs may potentially enable them to serve as magnetic biomaterials for future cancer treatment.

2. Experimental

2.1. Preparation of PVPylated Fe_3O_4 NPs

The pure Fe_3O_4 and PVPylated Fe_3O_4 NPs were formulated according to earlier reports.[26,27] Anhydrous ferric chloride ($FeCl_3$), urea and potassium hydroxide (KOH) were used as an initial precursor and base medium. Ethylene glycol (EG) and polyvinylpyrrolidone K-30 (PVP) were employed as the solvent and surfactant, respectively. In the typical solvothermal synthesis, 2.5 mM $FeCl_3$ was dissolved in 40 mL of EG. Then, 5 mM KOH and 0.5 mM urea were dissolved in 30 mL of EG. These two solutions were mixed well with continuous stirring at ambient temperature for 1 h to obtain a homogeneous solution. Following this, a required amount of PVP was added to the homogeneous solution and again stirred at room temperature for 30 min. The final solution was transferred into a 75 mL Teflon-lined stainless steel autoclave and heated at 210 °C for 15 h. Once the reaction was completed, a black suspension obtained was allowed to cool down at room temperature. The resultant black precipitates were collected using a strong external magnet and washed several times with deionized (DI) water and ethanol to remove impurities and unbound molecules. The resultant PVPylated Fe_3O_4 NPs were dried in a vacuum oven at 60 °C overnight.

2.2. Preparation of thymoquinone-loaded Fe_3O_4 NPs

TQ-PVP-Fe_3O_4 NPs were synthesised by a previously reported nanoprecipitation method with slight modifications.[26] Briefly, 200 mg PVPylated Fe_3O_4 NPs were suspended in 40 mL DI water and ultra-sonicated to acquire homogeneously dispersed particles. The pre-determined concentrations of 1-ethyl-3[3-dimethylaminopropyl]carbodiimide hydrochloride (EDC) and *N*-hydroxysuccinimide (NHS) were added and allowed for further ultra-sonication. Then, a required amount of thymoquinone was added and stirred at room temperature for 24 h. Finally, the resultant black precipitate was washed with DI water to remove the unloaded drug molecules. At the end of the process, TQ-PVP-Fe_3O_4 NPs were collected using a strong magnet applied externally and NPs were further dried in a vacuum oven.

2.3. Characterization

The phase purity and crystallinity of the pure Fe_3O_4, PVPylated Fe_3O_4 and TQ-PVP-Fe_3O_4 NPs were studied by X-ray diffraction (XRD, model D5005D, Germany). The chemical structure, functional groups and thymoquinone loading on PVPylated Fe_3O_4 NPs were analysed by Fourier transform infrared (FTIR) spectroscopy (FITR, Jasco Tensor 27, Japan). The surface micrograph of pure Fe_3O_4, PVPylated-Fe_3O_4 and TQ-PVP-Fe_3O_4 NPs were viewed using a field emission scanning electron

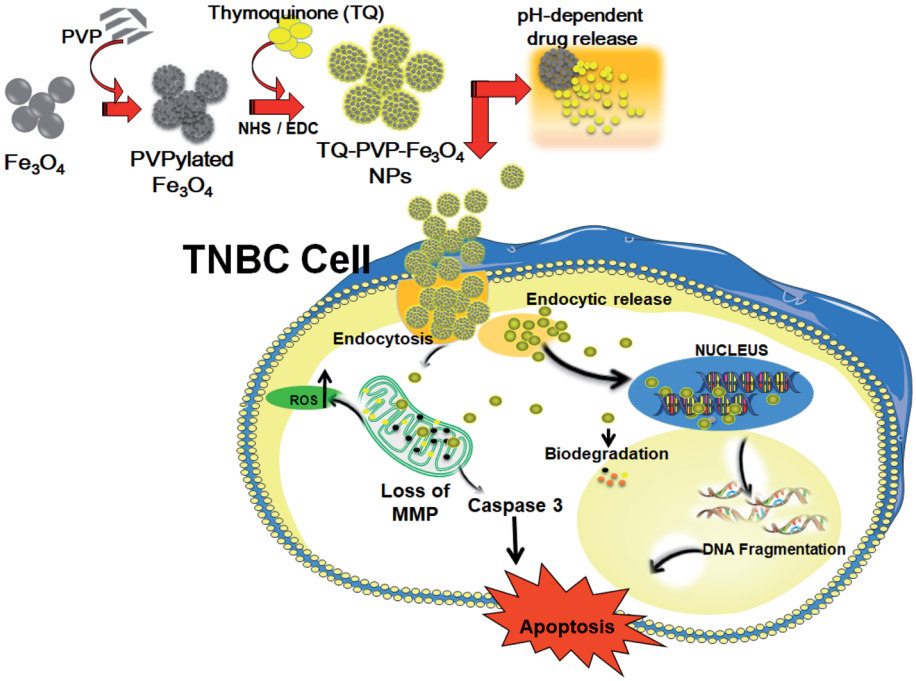

Scheme 1 Schematic of the formation and synthesis of pure Fe_3O_4, PVPylated Fe_3O_4, TQ-PVP-Fe_3O_4 NPs and their interaction and drug delivery behavior against triple-negative breast cancer cell line model.

microscope (FESEM, Quanta-250 FEG, Germany) with line scanning using an energy-dispersive X-ray spectrometer (EDX, Bruker, Germany) and transmission electron microscope (TEM, JEOL JEM-1200, Japan). The surface charge of magnetic NPs was measured using a zeta potential analyzer (Nicomp Zetasizer 380ZLS, USA). The weight loss and thermal stabilities of the pure Fe_3O_4, PVPylated-Fe_3O_4 and TQ-PVP-Fe_3O_4 NPs were measured by thermogravimetric analysis (TGA) under an oxygen gas flow (TA-TGA Q-500, TA Instrument, USA). A vibrating sample magnetometer (VSM, EV X model, USA) was used to measure the superparamagnetic behaviour of the pure Fe_3O_4 and drug-loaded Fe_3O_4 NPs at room temperature. The specific surface area, pore volume and pore size distribution of PVPylated Fe_3O_4 NPs were measured using a Brunner–Emmett–Teller surface area analyzer (BET, Microtarc, BELSORP-max, Japan).

2.4. MTT assay

The methyl thiazolyl tetrazolium (MTT) bromide assay was used to measure the cell viability in pure Fe_3O_4, PVPylated Fe_3O_4 and TQ-PVP-Fe_3O_4 NP-treated TNBC (MDA-MB-231) cells. Briefly, cultured cells were seeded in a 96-well plate at a density of 1×10^4 cells per well and incubated overnight. Then, these cells were treated with different concentrations of the prepared TQ-PVP-Fe_3O_4 NPs for 24 h. Then, the cells were treated with 100 μL per well of MTT solution (5 mg mL^{-1} concentration) and kept for incubation at 37 °C under dark conditions for another 4 h. The purple-colored formazan crystals produced from viable cells were dissolved in 100 μL of dimethyl sulfoxide. The absorbance was measured at 620 nm using a multi-well plate reader, and the observed values were expressed as a percentage relative to the respective control group.

2.5. Fluorescence microscopic analysis

By fluorescence microscopic analysis, the cellular internalization of NPs with cancer cells at different time points of incubation was studied. Briefly, RITC (rhodamine-B isothiocyanate)-labelled TQ-PVP-Fe_3O_4 NPs were treated and the level of internalization was quantified by fluorescence microscopy. Besides, rhodamine 123 (Rh 123)- and DAPI-stained cells were analyzed for the induction of apoptosis in cells, for which the MDA-MB-231 cells were cultured in 6-well plates at 37 °C with 5% CO_2 for 48 h. Then, the cells were treated with TQ-PVP-Fe_3O_4 NPs with different time intervals (0, 1, 2, 4 and 8 h). Following this, the medium was removed, and the NP-treated cells were gently washed twice with phosphate-buffered saline (PBS) and fixed in 3% paraformaldehyde for 20 min. The cells were re-washed with PBS and stained with 10 μg mL^{-1} 4′,6-diamidino-2-phenylindole (DAPI) at 37 °C in a dark place for 20 min. Consequently, the DAPI-stained cells were treated with 10 μg mL^{-1} Rh-123 at 37 °C for 30 min in the darkness. The cells were then washed with methanol and air dried and investigated for changes in $\Delta\Psi_m$ at an appropriate wavelength by fluorescence microscopy. The assessment of DNA damage in nuclear materials was performed by DNA fragmentation analysis using agarose gel electrophoresis.[8]

2.6. Assessment of reactive oxygen species (ROS)

By 2′,7′-dichlorfluorescein-diacetate (DCFH-DA) staining, the intracellular ROS production was analyzed using 2′,7′-

dichloroflorescein (DCF) signals from the dying cells. These observed DCF (green) fluorescence intensity was relatively proportional to the quantity of ROS generated from the dead cells. Briefly, the cells cultured in a six-well plate for 24 h were treated with TQ-PVP-Fe_3O_4 NPs at dose-dependent concentrations (20, 40, 60 and 80 μg mL^{-1}). Then, these cells were again washed with ice-cold PBS and incubated with DCFH-DA (50 μM in a final concentration) at 37 °C in the darkness for 30 min. Further, the cells were washed twice and sustained in 1 mL of PBS. ROS production was assessed using a fluorescence microscope at emission and excitation wavelengths of 530 nm and 488 nm, respectively, depending on the intensity of fluorescence as compared to the non-treated cells.

2.7. Statistical analysis

Data analyses were performed by Student's *t* test or one-way ANOVA using the GraphPad Prism 6.0 software. The error bars presented the mean ± standard deviation (SD) of three independent measurements ($n = 3$).

3. Results and discussion

The fabrication of TQ-PVP-Fe_3O_4 NPs involves three steps as depicted in Scheme 1. Primarily, the ferric chloride decomposes at high temperatures (210 °C) in a polyol medium, which results in the generation of Fe species that exclusively reacts with KOH in the closed reaction system to form monodisperse spherical Fe_3O_4 NPs. Similarly, the self-assembly of the primary seeded particles influences the building blocks of monodisperse porous shape by tuning homogeneous nucleation *via in situ* addition of PVPylated polymers. The *in situ* surface modification could improve water solubility, prolong the circulation time and impart a stealth-shielding shell. Further, the surfaces of PVPylated Fe_3O_4 NPs were modified with the active site by addition of NHS and EDC *via* ultra-sonication. Accordingly, the amino and carboxyl groups were used to impart to the surface the hydrophilic nature and tendency to encapsulate drug molecules.[26] Finally, the chosen drug thymoquinone (TQ) was uniformly loaded into the porous PVPylated Fe_3O_4 NPs *via* physical adsorption by the nanoprecipitation method to form TQ-PVP-Fe_3O_4 NPs. These TQ-PVP-Fe_3O_4 NPs were further studied to investigate their anticancer potentials in triple-negative breast cancer cells, and the interaction of NPs with cancer cells is presented in Scheme 1.

3.1. Structural characterization analysis

Powder X-ray diffraction (XRD) was used for evaluating the crystal structure and phase purity of Fe_3O_4, PVPylated Fe_3O_4 and TQ-PVP-Fe_3O_4 NPs (Fig. 1a). The obtained diffraction peaks of the samples were directly indexed to the cubic phase of Fe_3O_4 standards (JCPDS#: 89-3854) without impurities.[27,28] Scherer's formula was used to calculate the average crystalline size. The crystalline size of Fe_3O_4 NPs was approximately 21 nm, whereas the size of the particles was decreased to 18 and 16 nm for PVPylated Fe_3O_4 and TQ-PVP-Fe_3O_4 NPs, respectively. Moreover, it was found that the intensity of the corresponding XRD peaks decreased in PVPylated and TQ-PVP-Fe_3O_4 NPs due to the presence of amorphous materials (polymer/drugs) on their surface of Fe_3O_4 NPs. The corresponding XRD peaks did not show any induced peak shift and phase transition during the addition (*in situ*) of polymers or drug-loaded Fe_3O_4 NPs.

Further, the functional group and chemical structure of pure Fe_3O_4, PVPylated Fe_3O_4, pure thymoquinone and TQ-PVP-Fe_3O_4 NPs were analyzed by FTIR spectroscopy (Fig. 1b). It was found that pure Fe_3O_4 NPs exhibited strong and weak absorption peaks at 593 cm^{-1} and 466 cm^{-1} attributed to the Fe–O–Fe stretching vibration of the spinel structure. These absorption peaks confirmed the distribution of Fe ions in both octahedral and tetrahedral sites in the formation of Fe_3O_4 NPs.[27,28] Similarly, PVPylated Fe_3O_4 and TQ-PVP-Fe_3O_4 NPs showed the Fe–O bond in a slight shift towards lower wavenumber and sharp intensity peaks due to chemisorption of organic molecules.[29] In PVPylated Fe_3O_4 NPs, the broad peaks at 882 cm^{-1} and 1060 cm^{-1} could be ascribed to the CH_2 rocking and C–H stretching vibrations. In addition, the sharp intense peak at 1632 cm^{-1} represents the C=O stretching vibration, which further confirmed the successful wrapping of PVPylated and Fe_3O_4 NPs.[30] Moreover, the peaks at 2853 cm^{-1} and 2928 cm^{-1} could be assigned to the symmetric and asymmetric vibrations of $-CH_2$ molecules, respectively. The FTIR spectrum for pure thymoquinone has major peaks in the range of 600–1800 cm^{-1}, which substantiated the presence of carboxyl, hydroxyl, amide and aromatic groups.[31] The prominent peaks at 1031 cm^{-1} and 890 cm^{-1} could be assigned to the C=O stretching and C–H bending vibrations of the aromatic group, confirming the presence of TQ-PVP-Fe_3O_4 NPs. The obtained peaks at 1387 cm^{-1} and 1642 cm^{-1} could be assigned to the C–N stretching vibration of the amide group and the C=O stretching vibration of the carboxylic group, which closely matched with those of pure thymoquinone. Hence, it was confirmed that these obtained prominent peaks represent the successful loading of thymoquinone drug into PVPylated Fe_3O_4 NPs. In addition, all samples exhibited a broad peak at 3400–3450 cm^{-1}, which could be assigned to the O–H stretching vibration of hydroxyl groups. Thus, the FTIR spectral results confirmed the formation of the metal-oxide and the loading of drug molecules onto the surface of Fe_3O_4 NPs.

3.2. Field emission scanning electron microscopic (FESEM) analysis

The FESEM analysis of Fe_3O_4, PVPylated Fe_3O_4 and TQ-PVP-Fe_3O_4 NPs was performed at various magnifications, as displayed in Fig. 2a–i. The pure Fe_3O_4 NPs shown in Fig. 2a–c exhibit monodisperse agglomeration-free spherical structures with a smooth surface in the size range of 30–50 nm, which is clearly visible in highly magnified images. Due to the *in situ* addition of PVP, the NPs were shattered into small-sized nanocrystals and compactly packed with magnetic dipole interaction to form monodisperse porous hierarchical spherical structures, as represented in Fig. 2d–f. The size of the porous spherical structures was determined to be >100 nm with a number of ultra-small pores and voids. These pores were

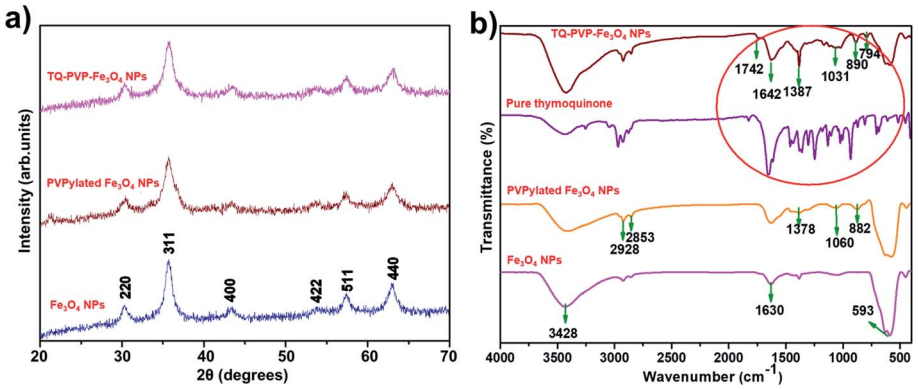

Fig. 1 (a) X-ray diffraction patterns of pure Fe_3O_4, PVPylated Fe_3O_4 and TQ-PVP-Fe_3O_4 NPs and (b) Fourier transform infrared spectra of pure Fe_3O_4, PVPylated Fe_3O_4, pure thymoquinone and TQ-PVP-Fe_3O_4 NPs. The circle indicates the corresponding thymoquinone FTIR peak matching with TQ-PVP-Fe_3O_4 NPs.

produced due to the uniform nucleation growth of organic–inorganic particles.[32] Thus, the higher surface energy would implement the aggregation of smaller crystals to form hierarchal nanostructures due to the Ostwald ripening process.[33] The nitrogen adsorption–desorption isotherm confirmed that the specific surface area, average pore size and pore volume of PVPylated Fe_3O_4 NPs (as shown in ESI Fig. S1†) were 68.70 m^2 g^{-1}, 5.27 nm and 0.0907 cm^3 g^{-1}, respectively. The FESEM image of TQ-PVP-Fe_3O_4 NPs is shown in Fig. 2g–i. The thymoquinone drug molecules were also uniformly loaded in porous nanostructures, and it was highlighted in the micrograph (Fig. 2i). The high surface area and nanometric pore size of

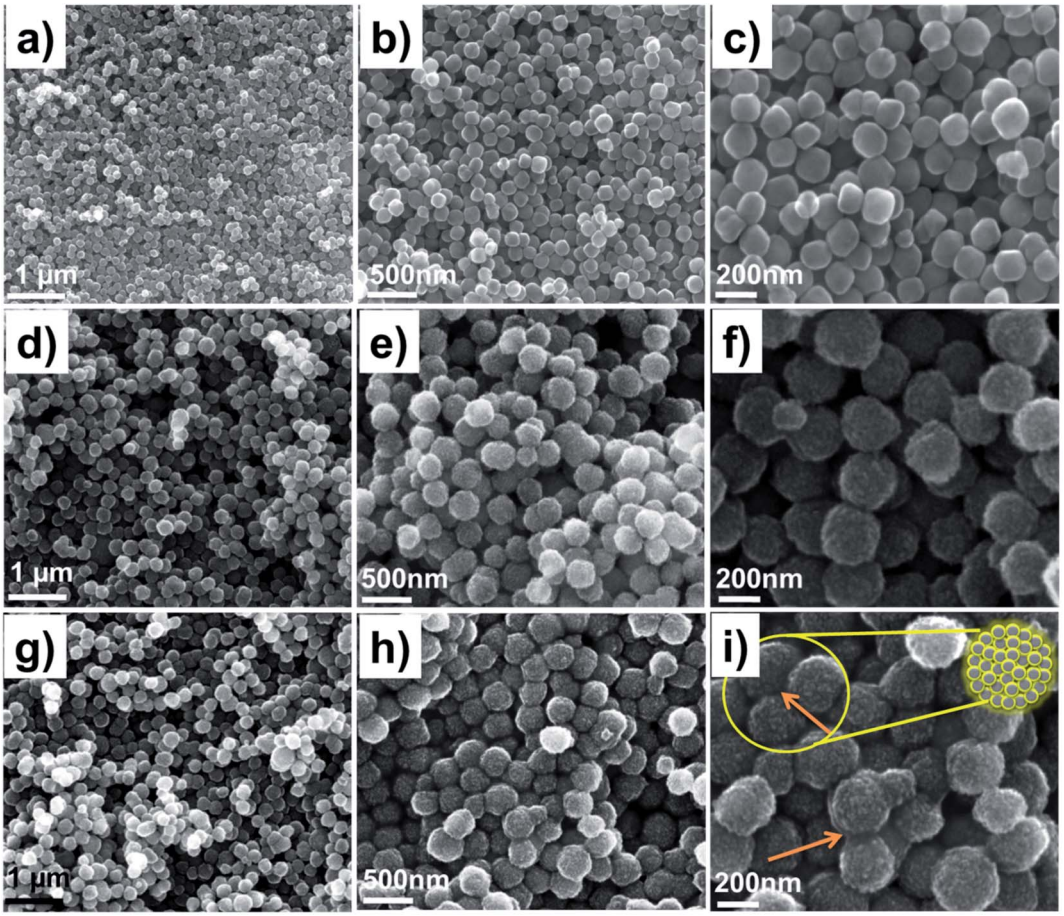

Fig. 2 Field emission scanning electron microscopic (FESEM) images of low and high magnifications for (a–c) pure Fe_3O_4, (d–f) PVPylated Fe_3O_4 and (g–i) TQ-PVP-Fe_3O_4 NPs (the inset in (i) represents the schematic diagram of thymoquinone loading effects on PVPylated Fe_3O_4 NPs).

PVPylated Fe_3O_4 could stimulate high thymoquinone drug loading *via* physical adsorption mechanism. Accordingly, the results of TQ-PVP-Fe_3O_4 NPs did not show any noteworthy changes in the shape or size when the drug was embedded into Fe_3O_4 NPs. This indicated that magnetic NPs did not show any significant changes such as dissolution or growth of nanocrystals during the drug loading or encapsulation process.[34]

A transmission electron microscope (TEM) was further used to confirm the morphologies of Fe_3O_4, PVPylated Fe_3O_4 and TQ-PVP-Fe_3O_4 NPs, as shown in Fig. 3a–c. The pure Fe_3O_4 NPs are monodisperse and spherical in shape in the size range of ~30–50 nm (Fig. 3a). Adding a structure directing agent, PVP, the monodisperse porous hierarchical spherical structures without agglomeration are clearly displayed in Fig. 3b. This porous nanostructure can adsorb more quantity of the thymoquinone drug (Fig. 3c) due to nanosized pore volume (Fig. S2†). The TEM morphologies further confirmed the successful thymoquinone loading in PVPylated Fe_3O_4 NPs.

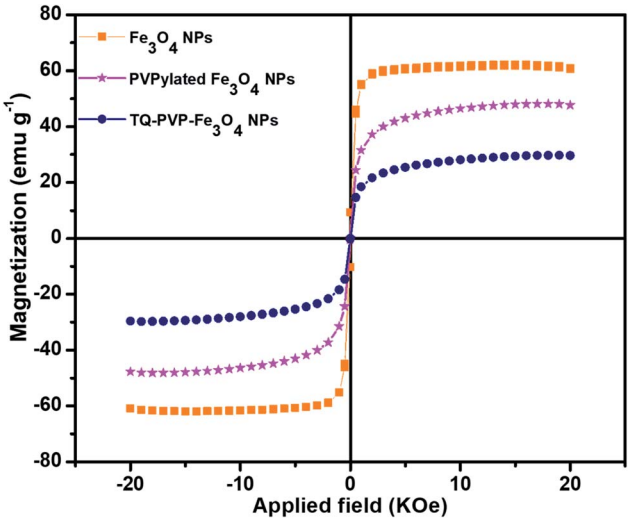

Fig. 4 Room temperature hysteresis loops for pure Fe_3O_4, PVPylated Fe_3O_4 and TQ-PVP-Fe_3O_4 NPs.

3.3. Analysis of magnetic properties

The magnetic properties of pure Fe_3O_4, PVPylated Fe_3O_4 and TQ-PVP-Fe_3O_4 NPs were studied using a vibrating sample magnetometer at room temperature with an applied magnetic field of 2*T* (Fig. 4). The absence of hysteresis loops with negligible coercivity and remanence implied that pure Fe_3O_4 NPs were superparamagnetic and did not alter the behavior of either PVPylated Fe_3O_4 or the loading of thymoquinone to their surface. The saturation magnetization (M_s) of pure Fe_3O_4 NPs was found to be 61 emu g^{-1} and the M_s value was slightly lower than the bulk counterpoint of 92 emu g^{-1}.[27] The energy of superparamagnetic particles in an applied field was directly proportional to their size *via* the number of magnetic molecules in a single magnetic domain. Moreover, if the energy of particles were compared with thermal energy, thermal fluctuations significantly reduce the total magnetic moments in a given field.[35] This might be a reason for decreasing the saturation magnetization of pure NPs by reducing the size when compared to bulk counterpoints. The M_s value was decreased to 48 emu g^{-1} for PVPylated Fe_3O_4 NPs. The presence of non-magnetic materials in Fe_3O_4 NPs decreased the M_s value due to the spin canting effect and smaller particle sizes.[5] In the case of TQ-PVP-Fe_3O_4 NPs, the M_s value was further decreased to 30 emu g^{-1}. The strong binding of amorphous thymoquinone drug shielded on the Fe_3O_4 NPs might be decreased in the effective magnetic moment due to an increase in the surface spin disorientation.[36] Therefore, the chemisorption of the non-magnetic layer quenched the M_s values and further confirmed the surface entrapment of the magnetic NPs. These results confirm that the changes in magnetic properties strongly depend on the size, shape and surface effects of Fe_3O_4 NPs.

3.4. Zeta potential measurements

The stability and dispersibility of Fe_3O_4 NPs depend on their surface chemistry, and it was studied by zeta potential analysis. Generally, the surface charge polarity of Fe_3O_4 NPs was changed by de-protonation and protonation effects, according to the following chemical equations.[37]

$$Fe–OH + H^+ \leftrightarrow Fe–OH_2^+ \text{ [protonation]}$$

$$Fe–OH \leftrightarrow Fe–O^- + H^+ \text{ [de-protonation]}$$

Based on the above reaction principle, the surface charges of Fe_3O_4 NPs were analyzed and the interaction of bio-molecules was studied. Thus, it was found that PVPylated Fe_3O_4 NPs showed negative surface charge (−24 mV) due to deprotonated surface effects, and TQ-PVP-Fe_3O_4 NPs exhibited a positive

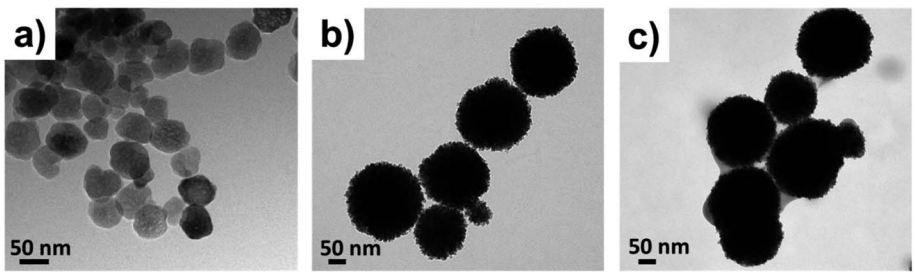

Fig. 3 Transmission electron microscopic (TEM) images of (a) pure Fe_3O_4, (b) PVPylated Fe_3O_4 and (c) TQ-PVP-Fe_3O_4 NPs.

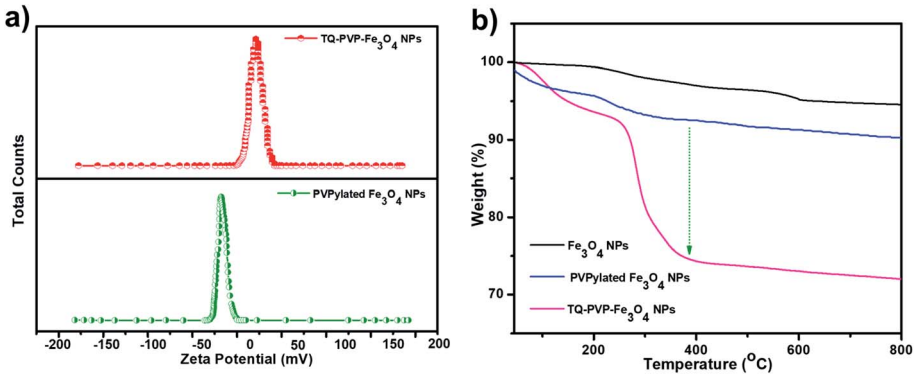

Fig. 5 (a) Zeta potential of PVPylated Fe_3O_4 and TQ-PVP-Fe_3O_4 NPs and (b) thermogravimetric measurements of pure Fe_3O_4, PVPylated Fe_3O_4 and TQ-PVP-Fe_3O_4 NPs.

surface charge of 6.1 mV (Fig. 5a). The change in surface charge confirms the strong interaction between the drug and Fe_3O_4 NPs. Moreover, it was well reported that the positively charged nanocarriers could easily bind to the negatively surface charged plasma membrane and gradually increase TQ-PVP-Fe_3O_4 NP uptake rates due to the electrostatic process.[38] Thus, the surface charge changed from positive to negative surface, confirming the successful loading of thymoquinone drug into PVPylated Fe_3O_4 NPs.

3.5. Thermal analysis

The amount of organic molecules adsorbed onto the surface of pure Fe_3O_4, PVPylated Fe_3O_4 and TQ-PVP-Fe_3O_4 NPs were quantified by thermogravimetric analysis (TGA) (Fig. 5b). The weight loss below 200 °C of all samples represents the desorption of water molecules. There was no significant weight loss with the increase in temperature, and this confirmed the high stability of pure Fe_3O_4 NPs. Upon addition of PVP to Fe_3O_4 NPs, slight weight loss (4.1%) was observed above 200 °C due to the decomposition of PVP molecules, and this observation was reported previously.[39] TQ-PVP-Fe_3O_4 NPs show two distinct weight losses corresponding to the strong binding of the thymoquinone drug and water molecules. The first weight loss of 7% was observed at a temperature of 50–250 °C due to the endothermic loss of surface hydroxyl groups[40] and the presence of PVP. Upon increasing the temperature above 250 °C, the second weight loss was obtained from the degradation of thymoquinone drug molecules. The high percentage of the weight loss was observed due to the strong wrapping of the drug as substantiated by the observation of 18.3% of thymoquinone drug loading in PVPylated Fe_3O_4 NPs. These results clearly indicated that thymoquinone could stably be loaded into Fe_3O_4 NPs. Finally, increasing the temperature above 400 °C resulted in no weight loss due to the strong Fe–O bond force constant, and therefore, more energy was required to effect the fracture of NPs.

3.6. Drug release profiles

The drug release behaviour under different pH conditions depends on the interior force between NPs and drug, size, surface behaviour, rate of dehydration and hydration of polymers. The *in vitro* drug release activity of TQ-PVP-Fe_3O_4 NPs was analysed in a phosphate buffer solution (pH 7.4) at a temperature of 37 °C to maintain the experimental condition similar to body fluids. The drug releasing profiles of TQ-PVP-Fe_3O_4 NPs were analysed by different pH conditions (4.6, 5.3 and 7.4). The two stages of drug release profiles were demonstrated such as early burst release under the basic condition and further fast release rate under acidic pH conditions, respectively. The thymoquinone release rate was primarily fast and becoming slower in extended time points (18 h). Initially, 26% of thymoquinone was released gradually (18 h) at pH 7.4. When decreasing the pH to 5.3 and 4.6, the drug release rate was rapid under acidic conditions. The thymoquinone release rate gradually increased and reached a maximum value of 74.5% and 85% in 18 h under two different acidic pH conditions (5.3 and 4.6), respectively (Fig. 6). In the acidic pH, the porous PVPylated Fe_3O_4 is exposed to acid etching, resulting in the expansion of pores that accelerates sustained drug release.[41] This pore expansion is attributed to high drug release in an acidic

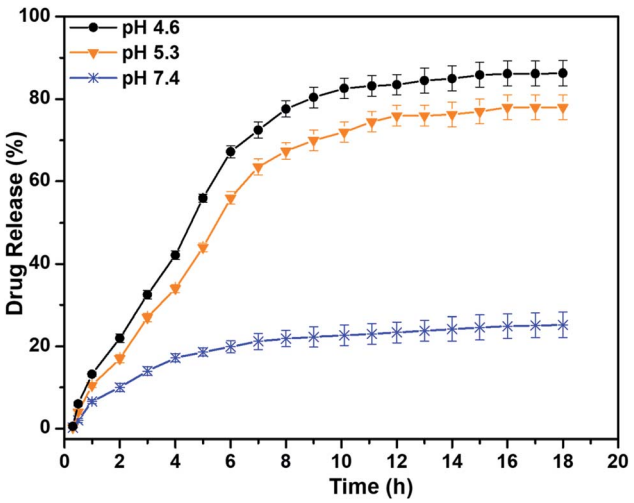

Fig. 6 Drug release profiles of TQ-PVP-Fe_3O_4 NPs under various pH conditions. The obtained values are expressed as mean ± SD ($n = 3$) of triplicate measurements.

environment, which could be due to the diffusion and swelling[42,43] of porous PVPylated Fe_3O_4 nanocarriers. Therefore, the thymoquinone release rate was attained efficiently under acidic conditions than under basic conditions. In addition, the *in vitro* drug release was depending not only on the pH-triggered release behaviour but also on the physicochemical properties of PVPylated Fe_3O_4 NPs.

3.7. *In vitro* anticancer analysis of TQ-PVP-Fe_3O_4 NPs

The MTT assay showed the cytotoxic effects of control, PVPylated Fe_3O_4, pure thymoquinone and TQ-PVP-Fe_3O_4 NPs in a chosen time point (24 h) against breast cancer (MDA-MB-231) cells (Fig. 7a). The cell viability percentages of TQ-PVP-Fe_3O_4 NP-treated cells were reduced as compared to that of control cells (untreated and drug-unloaded NPs). It was observed that the maximum concentrations of PVPylated Fe_3O_4 had no significant cytotoxicity in the cancer cells, and this confirmed the biocompatible property of NPs. The obtained inhibitory concentrations (IC_{50}) were 50 μg mL^{-1} for TQ-PVP-Fe_3O_4 NPs. This growth inhibition caused by TQ-PVP-Fe_3O_4 NPs was higher than that caused by pure thymoquinone due to the strong electrostatic interaction between the positively charged TQ-PVP-Fe_3O_4 NPs and the negatively charged MDA-MB-231 cell membranes.[12] This behavior enhances the NPs uptake as well as toxicity to cancerous cells as reported earlier.[44] Therefore, TQ-PVP-Fe_3O_4 NPs can cause high cytotoxicity to MDA-MB-231 cells in a dose-dependent manner. In addition, the fluorescence microscopic analysis of RITC-TQ-PVP-Fe_3O_4 NPs clearly indicated the time-dependent cellular internalization (0 h, 1 h, 2 h, 4 h and 8 h) and the level of uptake of NPs by cancer cells (Fig. 7b). The graph shows the mean fluorescence intensity of the internalized NPs by cancer cells (Fig. 7c). These data provide the evidence of TQ-PVP-Fe_3O_4 in tumor cell delivery due to effective cell internalization of NPs for promoting the event of apoptosis. Further, the results of this study clearly showed an increase in cytotoxicity of thymoquinone, and it was due to the sustained release of the loaded drug molecules from PVPylated Fe_3O_4 NPs and/or their more effective uptake by cells. The observations confirm the cytotoxic behavior of NPs in their wide range of concentration and the doses closes to IC_{50} values exhibit enhanced therapeutic abilities of TQ-PVP-Fe_3O_4 NPs.

3.8. Analysis of mitochondrial membrane potentials ($\Delta\Psi_m$) and DNA damage

The changes in mitochondrial membrane potential ($\Delta\Psi_m$) can be visualized by rhodamine-123 (Rh 123) staining. Rh 123 is a cationic fluorescent dye and can be retained by functional mitochondria with high $\Delta\Psi_m$. TQ-PVP-Fe_3O_4 NP-treated cells were stained with Rh-123 and the loss of $\Delta\Psi_m$ in cells was observed based on changes in their potentials after treating the cells with its IC_{50} for a period of 0, 1, 2, 4, and 8 h (Fig. 8). DAPI and Rh-123 were able to form fluorescent complexes with nuclear material and active mitochondrial membranes of the cells, respectively. Hence, these dyes were useful in detecting the apoptotic condensed nuclei and $\Delta\Psi_m$ loss. The study observations showed that TQ-PVP-Fe_3O_4 NP-treated cells revealed the diminished size of apoptotic nuclei (green + blue color) and the assembly of condensed chromatin at the periphery of the

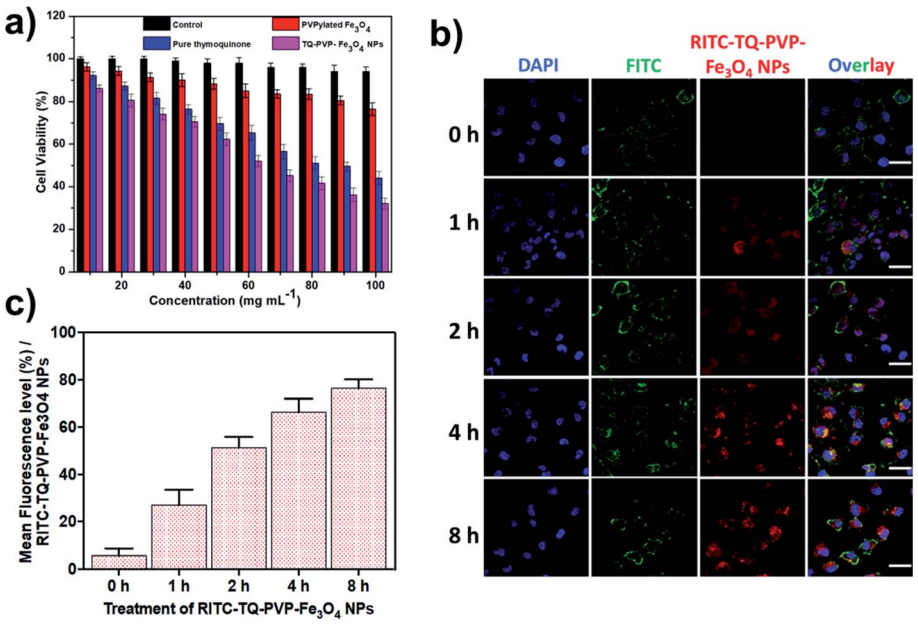

Fig. 7 (a) Cytotoxicity assessment results of control, PVPylated Fe_3O_4, pure thymoquinone and TQ-PVP-Fe_3O_4 NPs in MDA-MB-231 cells at different concentrations and the expressed values are mean ± SD ($n = 3$). (b) Fluorescence microscopic analysis of IC_{50} concentrations of RITC-TQ-PVP-Fe_3O_4 NPs in cellular internalization at different time intervals of incubation. DAPI (nucleus) and FITC (cell membrane) stains were used to cell organelles. Scale bars 50 μm. (c) Graph showing the quantified level of internalized NPs with cancer cells at different time points; the values were calculated depending on the mean fluorescence levels from RITC-TQ-PVP-Fe_3O_4 NPs.

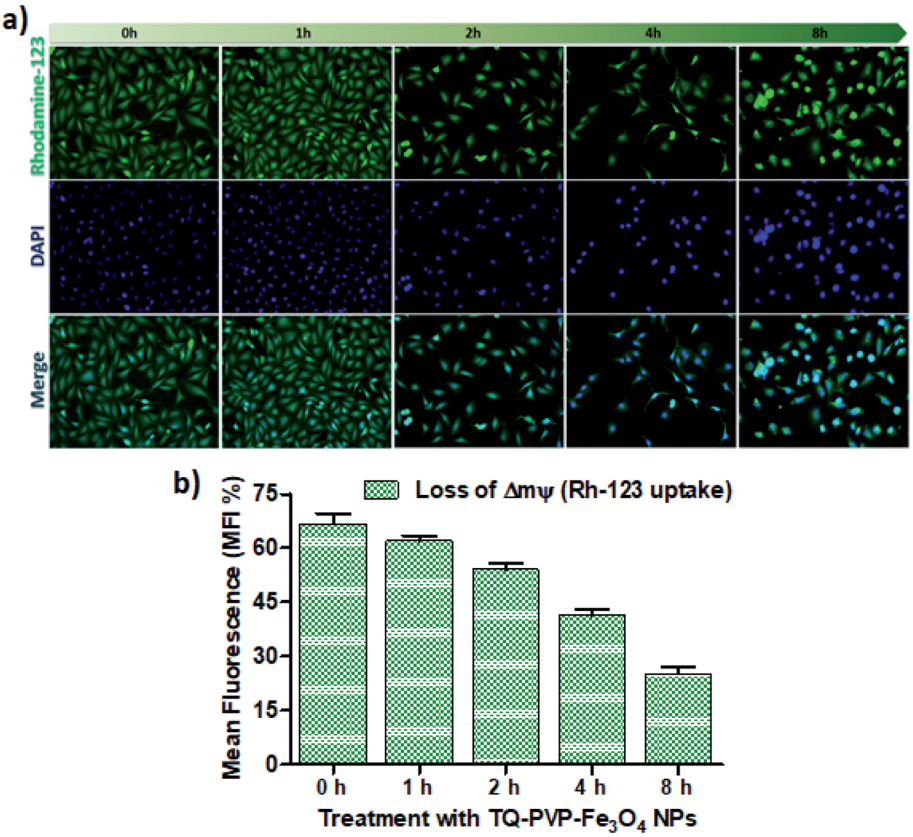

Fig. 8 (a) Fluorescence microscopic images (20× magnification) of DAPI and Rh-123-stained MDA-MB-231 cells treated with TQ-PVP-Fe_3O_4 NPs for different time periods. The panel of images shows the induction of apoptosis and loss of $\Delta\Psi_m$ in MDA-MB-231 cells; DAPI staining (blue color) shows the condensed and fragmented nuclear materials in TQ-PVP-Fe_3O_4 NP-treated cells as compared with untreated (control) cells; Rh-123 staining (green) indicates the loss of $\Delta\Psi_m$. The active mitochondrial membranes uptake Rh-123 and emit fluorescent green color and (b) quantitative analysis of loss of mitochondrial membrane potential based on the Rh-123 fluorescence level from MDA-MB-231 cells treated with TQ-PVP-Fe_3O_4 NPs.

nuclear membrane. The fragmented nuclear bodies and mitochondrial membranes were also observed in these cells. Besides, mitochondrial localization staining (Rh 123) of MDA-MB-231 cells treated with TQ-PVP-Fe_3O_4 NPs was observed in green color. The accumulation of fluorescence in MDA-MB-231 cells was also clearly visualized by fluorescence microscopy. These studies showed that TQ-PVP-Fe_3O_4 NPs induce mitochondrial membrane potential loss against MDA-MB-231 cancer cells. The quantitative analysis was performed to analyze the level of mitochondrial membrane potential loss as compared to lower time points (Fig. 8b). It was observed that there is an increased amount of Rh-123 uptake when the cells are exposed to prolonged duration (1 h, 2 h, 4 h and 8 h). It may happen due to the interaction of thymoquinone and surface receptors on the triple-negative breast cancer cells *via* surface functional groups[45,46] of NPs, which adversely affects the cellular function and phenotype and induces cell death and cancerous tissue apoptosis.

3.9. Reactive oxygen species generation and nuclear fragmentation

Further, we examined the release of reactive oxygen species (ROS) from TQ-PVP-Fe_3O_4 NP-treated MDA-MB-231 cells to confirm the activation of the apoptosis signaling cascade. These were assessed by fluorescent DCFH-DA staining from apoptosis-induced cells. It was noticed that there was an increased amount of DCF signals through esterase activity, which might be due to the release of peroxidase cytochrome c in the cytoplasm. This resulted in higher ROS production in TQ-PVP-Fe_3O_4 NP-treated MDA-MB-231 cells than untreated (control) cells. Similarly, the production of ROS was increased in TQ-PVP-Fe_3O_4 NP-treated MDA-MB-231 cells in a dose-dependent manner, as displayed in Fig. 9a–e. This ROS fluorescence level indicates the amount of ROS generation from cancer cells due to treatment with NPs at different concentrations (Fig. 9f). The increase in ROS production in a dose-dependent manner was observed by the increased fluorescent intensity of treated cells. These findings suggested that the increased release rate of ROS generation can cause $\Delta\Psi_m$ loss, which leads to the activation of intrinsic apoptosis cascade. It was also reported that the interaction of TQ-PVP-Fe_3O_4 NPs with MDA-MB-231 cells could induce oxidative stress through ROS production over the antioxidant defense strategies of cells.[44,46,47] Thus, these increased ROS levels in cancer cells resulted in a change of mitochondrial membrane integrity and oxidative stress-associated DNA

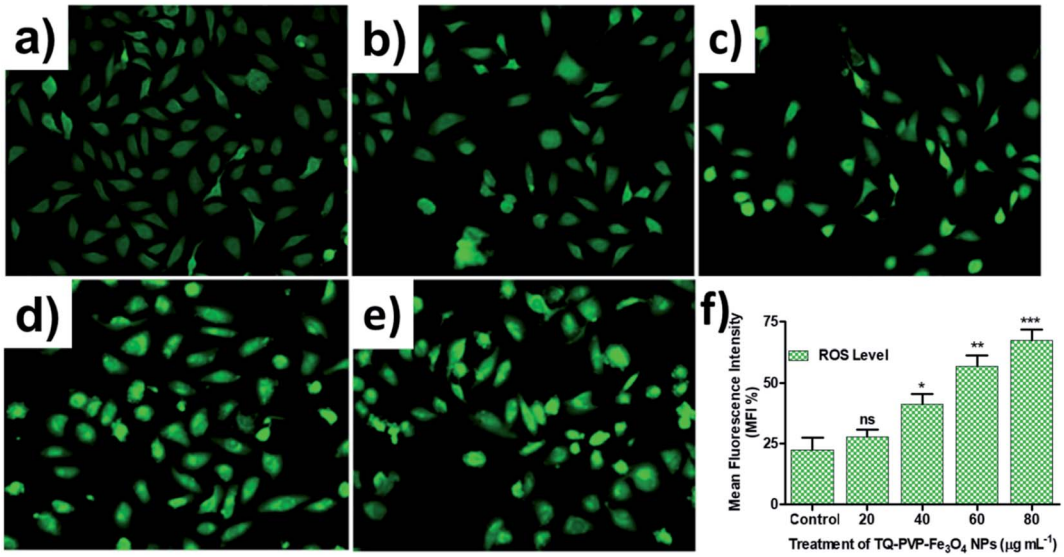

Fig. 9 Fluorescent microscopic images (40× magnification) of intra-cellular ROS production after TQ-PVP-Fe_3O_4 NP treatment under the conditions of (a) control, (b) at concentrations of 20, (c) 40, (d) 60, and (e) 80 μg mL^{-1} for 24 h, and (f) quantitative analysis of released ROS from MDA-MB-231 cells upon treatment with different concentrations of TQ-PVP-Fe_3O_4 NPs; the level of fluorescence is compared to the MFI of the respective control (untreated) cells after 24 h of treatment. ns = Non-significant; *p < 0.05; **p < 0.01; ***p < 0.001.

damage that could consequently lead to apoptosis.[12] These effects of TQ-PVP-Fe_3O_4 NPs on cellular ROS production were investigated under a fluorescent microscope for their potentials to show green fluorescence from DCF through the intracellular oxidation of DCFH-DA (fluorescent dye). In addition, it is shown that TQ-PVP-Fe_3O_4 NPs of this study have the potential to increase intracellular ROS levels as well as to activate intrinsic apoptosis.[44,46] Thus, the present study implies that the ROS generation and the associated oxidative stress induced by TQ-PVP-Fe_3O_4 NPs could effectively result in the activation of an intrinsic apoptotic pathway as revealed by extensive DNA damage of treated cancer cells and cell death (Scheme 1 and Fig. 10).

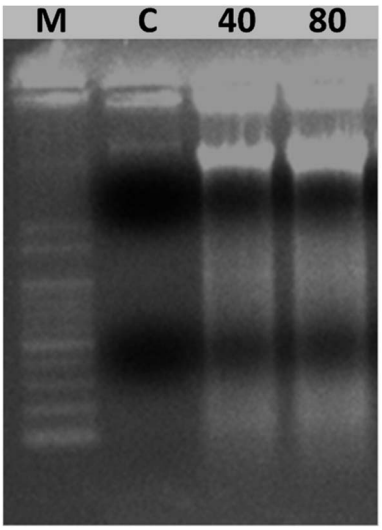

Fig. 10 DNA fragmentation analysis of control and TQ-PVP-Fe_3O_4 NP-treated MDA-MB-231 cells. The fragmented DNA samples are loaded as M-marker DNA, C-control, and TQ-PVP-Fe_3O_4 NPs at concentrations of 40 μg mL^{-1} and 80 μg mL^{-1}.

From the outcomes of this study, the enhanced mechanism of cellular uptake and growth inhibitory effects in MDA-MB-231 cells by TQ-PVP-Fe_3O_4 NPs was clearly demonstrated (as shown in Scheme 1). It was also assumed that TQ-PVP-Fe_3O_4 NPs effectively enter into the cellular system through the endocytosis process. The porous shape and positive zeta potential values play an important role in negatively charged tumor uptake and intracellular distribution. Then, TQ-PVP-Fe_3O_4 NPs might directly interact with the change in mitochondrial membrane potentials and agglomerate around the nuclear membrane of the nucleus.[45] In this biological environment, the thymoquinone drug may be released from PVPylated Fe_3O_4 NPs *via* disruption of weak van der Waals force.[12,26] Upon release, thymoquinone could accelerate apoptosis progression through DNA damage or membrane blebbing, resulting in cellular decomposition. In addition, TQ-PVP-Fe_3O_4 NPs possess high water solubility, good stability and increased anti-proliferation activity on tumor cells not only to enhance the drug index of the formulation but also to reduce the unwanted side effects of targeted drug delivery applications.

4. Conclusion

In summary, monodisperse porous PVPylated Fe_3O_4 NPs have been successfully synthesized by a solvothermal method. Thymoquinone was chosen as a model anticancer drug, which was loaded within porous PVPylated Fe_3O_4 NPs by the nanoprecipitation method. The FESEM morphological analysis confirmed the surface modification of magnetic NPs,

preventing the agglomeration as well as forming porous nanospheres with a size range of ~100 nm with superparamagnetic properties. The presence of PVPylated polymers could enhance water solubility, drug release and stability during the administration of TQ-PVP-Fe_3O_4 NPs. Moreover, it could deliver pre-determined encapsulated drugs more rapidly in an acidic pH environment as compared to a basic pH environment, showing the efficiency for rapid tumoricidal action. Anticancer studies of these Fe_3O_4 NPs demonstrated less toxic effects on MDA-MB-231 cells, whereas TQ-PVP-Fe_3O_4 NPs showed higher cytotoxicity. In addition, the particle size also played a vital role for targeting and releasing drug molecules in MDA-MB-231 cancer cells. It was also observed that TQ-PVP-Fe_3O_4 NP accumulation in tumor cells showed significant anticancer effects due to cellular decomposition and apoptosis. Hence, the developed method showed an effective manner of delivering water-insoluble therapeutic compounds to target cancer cells and enhance biological applications.

Conflicts of interest

There are no conflicts to declare.

Acknowledgements

The authors would like to acknowledge the DST-PURSE, DST-FIST and UGC-SAP, Government of India for the instrumental facilities to the department.

References

1 A. Diana, E. Franzese, S. Centonze, F. Carlino, C. M. Della Corte, J. Ventriglia, A. Petrillo, F. De Vita, R. Alfano and F. Ciardiello, Triple-negative breast cancers: systematic review of the literature on molecular and clinical features with a focus on treatment with innovative drugs, *Curr. Oncol. Rep.*, 2018, **20**(10), 76.

2 N. Olov, S. Bagheri-Khoulenjani and H. Mirzadeh, Combinational drug delivery using nanocarriers for breast cancer treatments: a review, *J. Biomed. Mater. Res., Part A*, 2018, **106**(8), 2272–2283.

3 Z. Xu, X. Chen, Z. Sun, C. Li and B. Jiang, Recent progress on mitochondrial targeted cancer therapy based on inorganic nanomaterials, *Mater. Today Chem.*, 2019, **12**, 240–260.

4 B. D. White, C. Duan and H. E. Townley, Nanoparticle Activation Methods in Cancer Treatment, *Biomolecules*, 2019, **9**(5), 202.

5 S. R. Kumar, M. Paulpandi, M. ManivelRaja, D. Mangalaraj, C. Viswanathan, S. Kannan and N. Ponpandian, An *in vitro* analysis of H1N1 viral inhibition using polymer coated superparamagnetic Fe_3O_4 nanoparticles, *RSC Adv.*, 2014, **4**(26), 13409–13418.

6 T. Vangijzegem, D. Stanicki and S. Laurent, Magnetic iron oxide nanoparticles for drug delivery: applications and characteristics, *Expert Opin. Drug Delivery*, 2019, **16**(1), 69–78.

7 M. Bilal, Y. Zhao, T. Rasheed and H. M. Iqbal, Magnetic nanoparticles as versatile carriers for enzymes immobilization: a review, *Int. J. Biol. Macromol.*, 2018, **120**, 2530–2544.

8 R. Vivek, R. Thangam, S. R. Kumar, C. Rejeeth, S. Sivasubramanian, S. Vincent, D. Gopi and S. Kannan, HER2 targeted breast cancer therapy with switchable "Off/On" multifunctional "Smart" magnetic polymer core–shell nanocomposites, *ACS Appl. Mater. Interfaces*, 2016, **8**(3), 2262–2279.

9 O. S. Fenton, K. N. Olafson, P. S. Pillai, M. J. Mitchell and R. Langer, Advances in biomaterials for drug delivery, *Adv. Mater.*, 2018, **30**(29), 1705328.

10 D. Bobo, K. J. Robinson, J. Islam, K. J. Thurecht and S. R. Corrie, Nanoparticle-based medicines: a review of FDA-approved materials and clinical trials to date, *Pharm. Res.*, 2016, **33**(10), 2373–2387.

11 S. K. Yen, P. Padmanabhan and S. T. Selvan, Multifunctional iron oxide nanoparticles for diagnostics, therapy and macromolecule delivery, *Theranostics*, 2013, **3**(12), 986.

12 S. Bhattacharya, M. Ahir, P. Patra, S. Mukherjee, S. Ghosh, M. Mazumdar, S. Chattopadhyay, T. Das, D. Chattopadhyay and A. Adhikary, PEGylated-thymoquinone-nanoparticle mediated retardation of breast cancer cell migration by deregulation of cytoskeletal actin polymerization through miR-34a, *Biomaterials*, 2015, **51**, 91–107.

13 M. A. Khan, M. Tania and J. Fu, Epigenetic role of thymoquinone: impact on cellular mechanism and cancer therapeutics, *Drug Discovery Today*, 2019, **24**, 2315–2322.

14 M. Rafati, A. Ghasemi, M. Saeedi, E. Habibi, E. Salehifar, M. Mosazadeh and M. Maham, *Nigella sativa* L. for Prevention of Acute Radiation Dermatitis in Breast Cancer: A Randomized, Double-blind, Placebo-controlled, Clinical Trial, *Complement. Ther. Med.*, 2019, 102205.

15 Y. K. Mahmoud and H. M. Abdelrazek, Cancer: thymoquinone antioxidant/pro-oxidant effect as potential anticancer remedy, *Biomed. Pharmacother.*, 2019, **115**, 108783.

16 M. Bule, S. Nikfar, M. Amini and M. Abdollahi, The Antidiabetic Effect of Thymoquinone: A Systematic Review and Meta-analysis of Animal Studies, *Food Res. Int.*, 2020, **127**, 108736.

17 M. Imran, A. Rauf, I. A. Khan, M. Shahbaz, T. B. Qaisrani, S. Fatmawati, T. Abu-Izneid, A. Imran, K. U. Rahman and T. A. Gondal, Thymoquinone: a novel strategy to combat cancer: a review, *Biomed. Pharmacother.*, 2018, **106**, 390–402.

18 O. R. Johnson-Ajinwo, A. Richardson and W.-W. Li, Synthesis and Evaluation of Thymoquinone Analogues as Anti-Ovarian Cancer Agents, *Proceedings*, 2019, **22**(1), 42.

19 R. Schneider-Stock, I. H. Fakhoury, A. M. Zaki, C. O. El-Baba and H. U. Gali-Muhtasib, Thymoquinone: fifty years of success in the battle against cancer models, *Drug Discovery Today*, 2014, **19**(1), 18–30.

20 M. Yusufi, S. Banerjee, M. Mohammad, S. Khatal, K. V. Swamy, E. M. Khan, A. Aboukameel, F. H. Sarkar and S. Padhye, Synthesis, characterization and anti-tumor

activity of novel thymoquinone analogs against pancreatic cancer, *Bioorg. Med. Chem. Lett.*, 2013, **23**(10), 3101–3104.

21 K. M. Sutton, C. D. Doucette and D. W. Hoskin, NADPH quinone oxidoreductase 1 mediates breast cancer cell resistance to thymoquinone-induced apoptosis, *Biochem. Biophys. Res. Commun.*, 2012, **426**(3), 421–426.

22 B. R. Acharya, A. Chatterjee, A. Ganguli, S. Bhattacharya and G. Chakrabarti, Thymoquinone inhibits microtubule polymerization by tubulin binding and causes mitotic arrest following apoptosis in A549 cells, *Biochimie*, 2014, **97**, 78–91.

23 W. H. Suriyah, A. R. Kasmuri, F. H. N. Foong, D. Afriza and S. J. A. Ichwan, Comparison of the *in vitro* and *in vivo* toxic effects of thymoquinone using oral cancer HSC-3 and HSC-4 cell lines, oral fibroblasts, HACAT cell line, and Zebrafish embryos, *Mater. Today: Proc.*, 2019, **16**, 2108–2114.

24 S. A. Helmy, M. El-Mesery, A. El-Karef, L. A. Eissa and A. M. El Gayar, Thymoquinone upregulates TRAIL/TRAILR2 expression and attenuates hepatocellular carcinoma *in vivo* model, *Life Sci.*, 2019, **233**, 116673.

25 M. Ogden, S. B. Karaca, G. Aydin, U. Yuksel, A. T. Dagli, S. Akkaya and B. Bakar, The Healing Effects of Thymoquinone and Dexpanthenol in Sciatic Nerve Compression Injury in Rats, *J. Invest. Surg.*, 2019, 1–9.

26 S. R. Kumar, S. Priyatharshni, V. Babu, D. Mangalaraj, C. Viswanathan, S. Kannan and N. Ponpandian, Quercetin conjugated superparamagnetic magnetite nanoparticles for *in vitro* analysis of breast cancer cell lines for chemotherapy applications, *J. Colloid Interface Sci.*, 2014, **436**, 234–242.

27 S. R. Kumar, V. Jayavignesh, R. Selvakumar, K. Swaminathan and N. Ponpandian, Facile synthesis of yeast cross-linked Fe_3O_4 nanoadsorbents for efficient removal of aquatic environment contaminated with As (v), *J. Colloid Interface Sci.*, 2016, **484**, 183–195.

28 S. R. Kumar, M. M. Raja, D. Mangalaraj, C. Viswanathan and N. Ponpandian, Surfactant free solvothermal synthesis of monodispersed 3D hierarchical Fe_3O_4 microspheres, *Mater. Lett.*, 2013, **110**, 98–101.

29 G. G. Utkan, F. Sayar, P. Batat, S. Ide, M. Kriechbaum and E. Pişkin, Synthesis and characterization of nanomagnetite particles and their polymer coated forms, *J. Colloid Interface Sci.*, 2011, **353**(2), 372–379.

30 S. R. Kumar, L. Marianna, S. Gianni, A. J. Nathanael, S. Hong, T. H. Oh, D. Mangalaraj, C. Viswanathan and N. Ponpandian, Hydrophilic polymer coated monodispersed Fe_3O_4 nanostructures and their cytotoxicity, *Mater. Res. Express*, 2014, **1**(1), 015015.

31 M. S. Al-Qubaisi, A. Rasedee, M. H. Flaifel, E. E. M. Eid, S. Hussein-Al-Ali, F. H. Alhassan, A. M. Salih, M. Z. Hussein, Z. Zainal, D. Sani, A. H. Aljumaily and M. I. Saeed, Characterization of thymoquinone/hydroxypropyl-β-cyclodextrin inclusion complex: Application to anti-allergy properties, *Eur. J. Pharm. Sci.*, 2019, **133**, 167–182.

32 B. Kong, J. Tang, Z. Wu, J. Wei, H. Wu, Y. Wang, G. Zheng and D. Zhao, Ultralight mesoporous magnetic frameworks by interfacial assembly of prussian blue nanocubes, *Angew. Chem., Int. Ed.*, 2014, **53**(11), 2888–2892.

33 H. Qu, D. Caruntu, H. Liu and C. J. O'Connor, Water-dispersible iron oxide magnetic nanoparticles with versatile surface functionalities, *Langmuir*, 2011, **27**(6), 2271–2278.

34 C. S. Lee, H. H. Chang, P. K. Bae, J. Jung and B. H. Chung, Bifunctional Nanoparticles Constructed Using One-Pot Encapsulation of a Fluorescent Polymer and Magnetic (Fe_3O_4) Nanoparticles in a Silica Shell, *Macromol. Biosci.*, 2013, **13**(3), 321–331.

35 K. V. Shafi, A. Gedanken, R. Prozorov and J. Balogh, Sonochemical preparation and size-dependent properties of nanostructured $CoFe_2O_4$ particles, *Chem. Mater.*, 1998, **10**(11), 3445–3450.

36 S. Ghosh, A. Badruddoza, M. Uddin and K. Hidajat, Adsorption of chiral aromatic amino acids onto carboxymethyl-β-cyclodextrin bonded Fe_3O_4/SiO_2 core–shell nanoparticles, *J. Colloid Interface Sci.*, 2011, **354**(2), 483–492.

37 P. Papaphilippou, M. Christodoulou, O.-M. Marinica, A. Taculescu, L. Vekas, K. Chrissafis and T. Krasia-Christoforou, Multiresponsive polymer conetworks capable of responding to changes in pH, temperature, and magnetic field: synthesis, characterization, and evaluation of their ability for controlled uptake and release of solutes, *ACS Appl. Mater. Interfaces*, 2012, **4**(4), 2139–2147.

38 S.-H. Wu, Y. Hung and C.-Y. Mou, Mesoporous silica nanoparticles as nanocarriers, *Chem. Commun.*, 2011, **47**(36), 9972–9985.

39 S. Afzal, R. Khan, T. Zeb, M. ur Rahman, S. Ali, G. Khan, Z. ur Rahman and A. Hussain, Structural, optical, dielectric and magnetic properties of PVP coated magnetite (Fe_3O_4) nanoparticles, *J. Mater. Sci.: Mater. Electron.*, 2018, **29**(23), 20040–20050.

40 J. Zheng, Z. Liu, X. Zhao, M. Liu, X. Liu and W. Chu, One-step solvothermal synthesis of Fe_3O_4@C core–shell nanoparticles with tunable sizes, *Nanotechnology*, 2012, **23**(16), 165601.

41 K. Cheng, S. Peng, C. Xu and S. Sun, Porous hollow Fe_3O_4 nanoparticles for targeted delivery and controlled release of cisplatin, *J. Am. Chem. Soc.*, 2009, **131**(30), 10637–10644.

42 S. Bhattacharya, A. Ghosh, S. Maiti, M. Ahir, G. H. Debnath, P. Gupta, M. Bhattacharjee, S. Ghosh, S. Chattopadhyay and P. Mukherjee, Delivery of thymoquinone through hyaluronic acid-decorated mixed Pluronic® nanoparticles to attenuate angiogenesis and metastasis of triple-negative breast cancer, *J. Controlled Release*, 2020, **322**, 357–374.

43 P. Upadhyay, S. Sarker, A. Ghosh, P. Gupta, S. Das, M. Ahir, S. Bhattacharya, S. Chattopadhyay, S. Ghosh and A. Adhikary, Transferrin-decorated thymoquinone-loaded PEG-PLGA nanoparticles exhibit anticarcinogenic effect in non-small cell lung carcinoma *via* the modulation of miR-34a and miR-16, *Biomater. Sci.*, 2019, **7**(10), 4325–4344.

44 E.-S. A. Arafa, Q. Zhu, Z. I. Shah, G. Wani, B. M. Barakat, I. Racoma, M. A. El-Mahdy and A. A. Wani, Thymoquinone

up-regulates PTEN expression and induces apoptosis in doxorubicin-resistant human breast cancer cells, *Mutat. Res., Fundam. Mol. Mech. Mutagen.*, 2011, **706**(1–2), 28–35.

45 M. Shah, N. Ullah, M. H. Choi, M. O. Kim and S. C. Yoon, Amorphous amphiphilic P (3HV-*co*-4HB)-*b*-mPEG block copolymer synthesized from bacterial copolyester *via* melt transesterification: nanoparticle preparation, cisplatin-loading for cancer therapy and *in vitro* evaluation, *Eur. J. Pharm. Biopharm.*, 2012, **80**(3), 518–527.

46 R. Thangam, S. Sundarraj, R. Vivek, V. Suresh, S. Sivasubramanian, M. Paulpandi, S. V. Karthick, A. S. Ragavi and S. Kannan, Theranostic potentials of multifunctional chitosan–silver–phycoerythrin nanocomposites against triple negative breast cancer cells, *RSC Adv.*, 2015, **5**(16), 12209–12223.

47 A. H. El-Far, S. K. Al Jaouni, W. Li and S. A. Mousa, Protective roles of thymoquinone nanoformulations: Potential nanonutraceuticals in human diseases, *Nutrients*, 2018, **10**(10), 1369.